Nano Research 2016, 9(7): 2174–2181
DOI 10.1007/s12274-016-1106-x
Research Article
ISSN 1998-0124
CN 11-5974/O4

Meso-porous silicon-coated carbon nanotube as an anode for lithium-ion battery

Won-Sik Kim, Jonghyun Choi, and Seong-Hyeon Hong (✉)

Department of Materials Science and Engineering and Research Institute of Advanced Materials, Seoul National University, Seoul 151-744, Republic of Korea

Received: 15 February 2016
Revised: 12 April 2016
Accepted: 17 April 2016

© Tsinghua University Press and Springer-Verlag Berlin Heidelberg 2016

KEYWORDS
Si,
meso-porous,
carbon nanotube (CNT),
magnesiothermic reduction,
battery

ABSTRACT

Meso-porous Si-coated carbon nanotube (CNT) composite powders were prepared by combining a sol–gel method and the magnesiothermic reduction process. Meso-porous Si-coated CNT electrodes exhibit excellent cycle and rate performances as anodes in Li-ion batteries (LIBs), which can be attributed to the efficient accommodation of volume change from meso-porous Si structure and the enhanced electrical conductivity from CNT core. This simple synthesis and subsequent reduction process provide a scalable route for the large-scale production of Si-C composite nanostructures, which can be utilized in a variety of applications, such as in photocatalysis, photoelectrochemical cells (PECs), and LIBs.

1 Introduction

Si is a promising alternative anode material to graphite, which is conventionally used in Li-ion batteries (LIBs), because of its high theoretical capacity (~4,200 mAh·g^{-1}), non-toxicity, and abundance [1, 2]. However, the rapid capacity fading exhibited by Si electrodes, which results from the structural pulverization caused by large volume expansion (up to 300%) during lithiation/delithiation, hinders their practical applications. To overcome this limitation, various Si nanostructures have been fabricated, including nanoparticles, nanowires, nanosheets, hollow spheres, porous structures, and core–shells [3–9]. Among them, carbon nanotube (CNT)@Si core–shell electrodes have shown impressive electrochemical properties, with the CNT core providing mechanical strength and electronic conductivity and the Si shell delivering high capacity [10–12]. Si-CNT composites can be further extended to produce various hybrid structures, such as nanosponges, flexible fabrics, and free-standing core–shell structures [13–18].

Although CNT@Si electrodes have been shown to have excellent reversible capacity and cycle performance, the fabrication of such electrodes commonly requires complicated procedures involving toxic precursors or expensive techniques. Recently, a low-

Address correspondence to shhong@snu.ac.kr

temperature magnesiothermic reduction was employed to convert various three-dimensional (3-D) SiO_2 structures into micro-porous or meso-porous nano-crystalline Si materials while preserving the original shape [6, 19–22]. The Si replicas possessed high specific surface areas and abundant inner space, which help to buffer the large volume expansion that occurs when such materials are used as anodes for LIBs. The magnesiothermic reduction process has been applied to prepare CNT@Si composites, but the SiO_2 layer on the CNTs is typically converted into Si nanoparticles with a low mass loading [23], or unexpected SiC and Mg_2SiO_4 phases form in addition to Si [24]. SiC is known to be inactive in LIBs, although the graphitized doped 6H-SiC has been recently shown to be activated for lithiation [25]. In addition, when unexpected Mg_2Si is formed as an intermediate phase during the reduction process, micro-sized clumpy Si is obtained as a final product, resulting in poor cyclability [22]. Thus, the preparation and electrochemical performance of as-reduced CNT@Si composites have not been thoroughly characterized. In addition, the ramping rate has been reported to significantly affect the morphology of as-reduced Si, with a high ramping rate resulting in a violent reaction and the ejection of reactants [26]. Consequently, controlling the ramping rate and annealing temperature is highly desirable for obtaining nano-porous or meso-porous CNT@Si core–shell electrodes via magnesiothermic reduction.

In this study, we investigate the preparation of meso-porous Si-coated CNTs (CNT@mp-Si) derived from CNT@SiO_2 core–shell structures by magnesiothermic reduction to develop the process conditions required to produce large amounts of meso-porous Si-coated CNTs. Additionally, the electrochemical performances of meso-porous Si with/without the CNT core are compared. The smooth surface of the SiO_2 shell is transformed into a meso-porous Si shell after the reduction and acid treatment. The obtained CNT@mp-Si electrode exhibits reversible capacities of 1,310 mAh·g^{-1} at 500 mA·g^{-1} after 100 cycles and 1,019 mAh·g^{-1} at 1,000 mA·g^{-1} after 300 cycles.

2 Experimental

2.1 Synthesis of CNT@SiO_2 core–shell structures

CNTs were purified in nitric acid at 140 ℃ for 10 h. After washing with deionized (D.I.) water and drying, 0.05 g of acid-treated CNTs was dispersed in 120 mL of ethanol and 30 mL of D.I. water. Then, 2.5 mL of ammonia solution (28%) was added under mild stirring. Subsequently, 6 mL of tetraethyl orthosilicate (TEOS) was added to 60 mL of ethanol, and this solution was mixed with the CNT dispersion. After stirring for 2 h, the products were centrifuged, washed with D.I. water, dried, and calcined at 600 ℃ for 1 h under a 5% H_2/N_2 atmosphere.

2.2 Reduction of CNT@SiO_2 to CNT@mp-Si

First, 0.5 g of calcined CNT@SiO_2 and 0.45 g of Mg (Sigma Aldrich) were mixed by hand. The mixture was heated at 400 ℃ for 2 h and then at 750 ℃ for 4 h under a 5% H_2/N_2 atmosphere. The ramping rate was fixed at 5 ℃/min. The obtained brown products were washed with HCl and HF solutions and dried at 80 ℃ in a vacuum oven.

2.3 Electrochemical test

The 2032 coin–type cells (Welcos, Korea) were assembled in an Ar-filled glove box, and pure Li foil was used as an electrode. The working electrode was fabricated by compressing a mixture of the active materials (CNT@mp-Si and mp-Si nanotubes), a conductive material (super P), and a binder consisting of polyacrylic acid (PAA)/carboxymethyl cellulose (CMC) (1/1) in a 60:20:20 weight ratio onto Cu foil with an active material loading of 0.9–1.4 mg·cm^{-2}. The electrode was dried at 80 ℃ for 12 h in an oven. A microporous film was used as the separator (Celgard). The electrolyte was $LiPF_6$ (1 M) and fluoroethylene carbonate (10%, FEC) in ethylene carbonate/diethyl carbonate (EC/DEC) (3:7 v/v). The cells were galvanostatically charged and discharged between 0.04 and 1.5 V versus Li^+/Li at room temperature in a program-controlled battery test system (WBCS 3000S WonATech). The specific capacity was calculated based on the composite weight.

3 Results and discussion

The synthesis procedure for CNT@mp-Si is schematically shown in Scheme 1. The as-received CNTs were purified

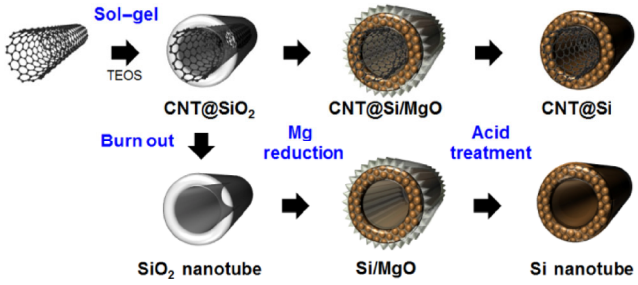

Scheme 1 Schematic illustration of the synthesis of CNT@mp-Si and meso-porous Si nanotubes.

with nitric acid by reflux. The acid-treated CNTs have modified surfaces, leading to the heterogeneous nucleation of SiO_2. The CNTs were coated with SiO_2 via a simple sol–gel method using TEOS without a surfactant. After washing with D.I. water and drying, the CNT@SiO_2 core–shell structure was calcined at 600 ℃ under a 5% H_2/N_2 atmosphere to remove any organic residue. Magnesiothermic reduction was employed to convert the SiO_2 shell into meso-porous Si (mp-Si). A two-step reduction process (400 and 750 ℃) was adopted in this study to avoid a violent reaction (burst) and to achieve a uniform coating (see the Electronic Supplementary Material (ESM), Fig. S1). Subsequently, the reduction product (MgO) and unreacted SiO_2 were subjected to a two-step etching procedure using HCl and HF solutions, generating in CNT@mp-Si. For comparison, meso-porous Si nanotubes (mp-Si nanotubes) were prepared by burning the CNT core out of the CNT@SiO_2 core–shell structure in an air atmosphere and then following the rest of the experimental procedure as described. The additional calcination step at 400 ℃ is a crucial factor to ensure a uniform magnesiothermic reduction process. Without this step, the mixture of reactants tends to explode, yielding an inhomogeneous reaction and unexpected second phases, such as Mg_2Si and Mg_2SiO_4 (see the ESM, Figs. S2 and S3). In a previous study [26], no ejection of the reactants occurred below a ramping rate of 5 ℃·min^{-1}, at which the reactants are violently ejected, possibly because of the different amounts of loaded sample. Another experiment revealed that the ejection of powder starts at 450 ℃ and that the ejected powder is composed of Si, Mg, Mg_2Si, and Mg_2SiO_4. These species are obtained after calcination at 750 ℃ without the intermediate calcination step (see the ESM, Figs. S3 and S4). The ejection of the powder is believed to result from local heat accumulation and SiO gas generation via the following reactions

$$3Mg(s) + 2SiO_2(s) = 3MgO(s) + SiO(g) + Si(s)$$

$$5Mg(s) + 2SiO_2(s) = 3MgO(s) + SiO(g) + Mg_2Si(s).$$

These reactions are thermodynamically favorable at the reaction temperatures (see the ESM, Fig. S5), and thus, the local heat accumulation and trapped SiO gas might be primarily responsible for the exploding reaction. Thus, the calcination at 400 ℃ may facilitate the slow release of the accumulated local heat and generated SiO gas, thereby inhibiting the violent reaction and secondary phase formation and leading to the desired mixture of Si and MgO at magnesiothermic temperatures, such as 750 ℃.

The phase developments during magnesiothermic reduction and acid etching were examined by X-ray diffraction (XRD), and the patterns of the SiO_2-coated, as-reduced, HCl-treated, and HF-treated CNTs are shown in Fig. 1(a). No diffraction peak can be observed for CNT@SiO_2 indicating that the as-coated SiO_2 is amorphous. The as-reduced specimen is composed of Si and MgO, which implies the successful reduction of SiO_2 by Mg. MgO and unreacted amorphous SiO_2 are completely dissolved during acid leaching, producing crystalline Si. The obtained CNT@Si material was further characterized by X-ray photoelectron spectroscopy (XPS) (Fig. 1(b)). The survey spectrum shows that the specimen is composed of Si, C, and O. The appearance of the O 1s peak can be attributed to the formation of a native oxide, despite etching CNT@Si HF. The high-resolution and deconvoluted spectra reveal that Si 2p is mainly Si^0 (Si $2p_{3/2}$ at 99.08 eV and Si $2p_{1/2}$ at 99.8 eV), with a minor amount of Si^{4+} (at 103.4 eV). The presence of the Si^{4+} peak indicates that a small amount of SiO_2 is present in the prepared CNT@mp-Si. Thus, the CNT@mp-Si core–shell structure was successfully fabricated by sol–gel coating and magnesiothermic reduction.

The morphology changes during magnesiothermic reduction and acid etching were observed by field emission scanning electron microscopy (FE-SEM). The SEM images of the as-received CNTs and acid-treated CNTs are shown in Figs. 2(a) and 2(b), respectively.

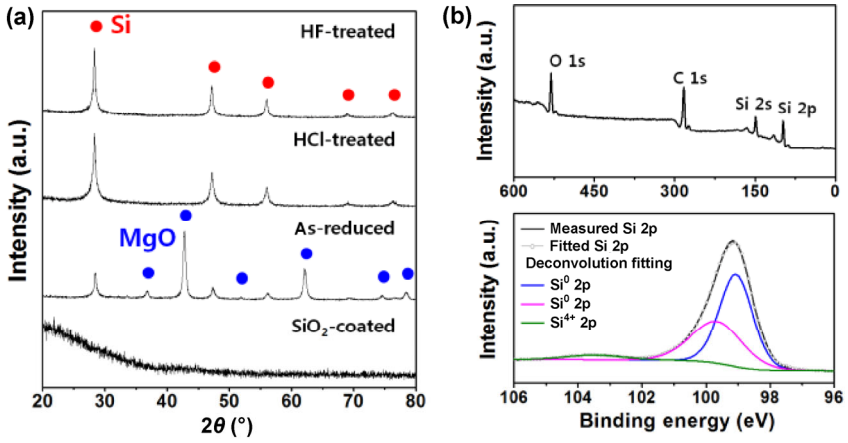

Figure 1 (a) XRD patterns of SiO_2-coated, as-reduced, HCl-treated, and HF-treated CNTs; (b) XPS of CNT@mp-Si powder.

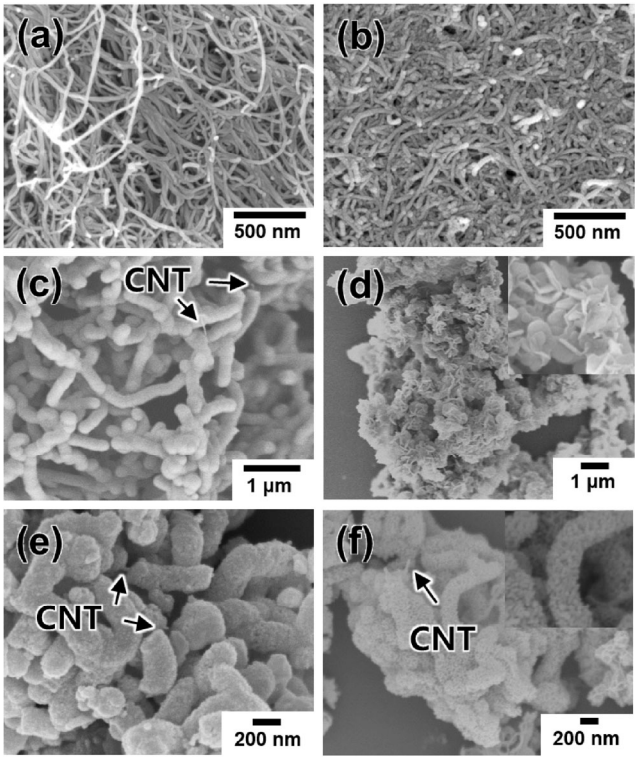

Figure 2 SEM images of (a) the as-received CNTs, (b) acid-treated CNTs, (c) SiO_2-coated CNTs, (d) as-reduced CNT@mp-Si-MgO composite, (e) HCl-treated CNT@mp-Si, and (f) HF-treated CNT@mp-Si.

After acid treatment, the CNTs had a slightly rough surface, but the diameters were not substantially changed. The SEM image of the SiO_2-coated CNTs shows that an amorphous SiO_2 layer was uniformly coated on the surface of CNTs with a thickness of 200 nm (Fig. 2(c)). The occasional observation of partially coated CNTs, marked by arrows, clearly indicates the conformal coaxial coating of SiO_2 on the CNTs. After magnesiothermic reduction, the specimen was highly agglomerated and covered with abundant MgO nanoplates and thus, no 1-D structure can be clearly distinguished (Fig. 2(d)). The formation of MgO nanoplates indicates that Mg vapor is generated during that reduction process and that MgO nanoplates formed via a vapor-phase reaction. The 1-D structure reappeared after dissolving the MgO in HCl (Fig. 2(e)), and CNT@mp-Si were finally obtained after HF treatment (Fig. 2(f)). The diameter of CNT@mp-Si was similar to that of the CNT@SiO_2 core–shell structure, and thus, the original morphology was preserved. The presence of the CNT core in the obtained CNT@mp-Si can be seen in the partially coated CNTs marked by arrows. Based on thermogravimetric analysis (TGA), the carbon content of CNT@mp-Si was estimated to be 23 wt.%. (see the ESM, Fig. S6).

The meso-porous structure was further confirmed by transmission electron microscopy (TEM), which revealed that the primary Si crystallites are approximate 5 nm in size and that the meso-pores have diameters in the range of 5–10 nm, similar to previously reported values (Figs. 3(a) and 3(b)) [20]. The selected-area diffraction (SAED) pattern was indexed to Si (ICDD #27-1402), and the ring pattern indicates the randomly oriented polycrystalline nature of mp-Si (Fig. 3(c)). The high-magnification TEM image also shows a few nanometer-sized Si grains (Fig. 3(d)). These results show that well-crystallized, meso-porous, Si-coated CNTs were synthesized from SiO_2@CNT core–shell structures via a facile magnesiothermic reduction

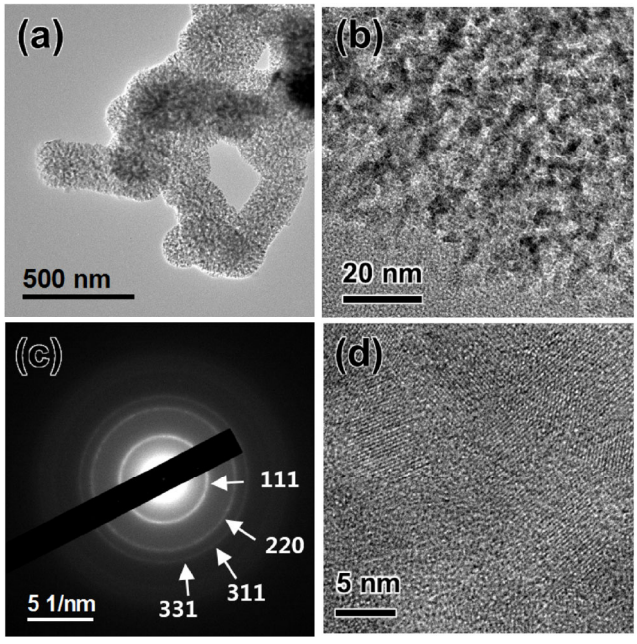

Figure 3 (a) and (b) Low-magnification TEM images, (c) SAED pattern, and (d) high-magnification TEM image of CNT@mp-Si.

reaction. As mentioned, mp-Si nanotubes can also be simply prepared by following the same procedure but burning away the CNT core in an air atmosphere before mixing with Mg powder. The phase of the obtained mp-Si nanotubes is crystalline Si, and the surface morphology is similar to that of CNT@mp-Si (see the ESM, Fig. S7).

The charge/discharge voltage profile of the CNT@mp-Si electrode between 0.04 and 1.5 V at current densities of 200 $mA·g^{-1}$ (first cycle) and 500 $mA·g^{-1}$ (subsequent cycles) are shown in Fig. 4(a). A long, flat plateau is observed in the first discharge (lithiation) curve, which corresponds to the Li-alloying of crystalline Si to form amorphous Li_xSi [27]. The subsequent charge (lithiation) and discharge (delithiation) curves exhibit the characteristics of amorphous Si [28–30]. The first charge and discharge capacities of the CNT@mp-Si electrode are 2,735 and 1,601 $mAh·g^{-1}$, respectively, at a current density of 200 $mA·g^{-1}$, corresponding to a coulombic efficiency of 59%. The irreversible capacity loss is associated with the formation of a solid electrolyte interphase (SEI) and the irreversible surface oxidation reaction of Li^+ on mesoporous Si. When the current density is increased to 500 $mA·g^{-1}$, the charge and discharge capacities are 1,445 and 1,323 $mAh·g^{-1}$, respectively. Both capacities decreased up to the 5th cycle and then gradually increased up to the 50th cycle. The electrochemical performance of the CNT@mp-Si electrode was evaluated by cyclic voltammetry (CV) in a potential range of 0.01–1.5 V versus Li^+/Li at a scan rate of 0.04 $mV·s^{-1}$ (see the ESM, Fig. S8). The CV curve exhibits lithiation and delithiation peaks at potentials typical of Si anodes [26]. The lithiation peaks at 0.21 and 0.1 V are ascribed to the transformation of crystalline Si to amorphous Li-Si. The two delithiation peaks at 0.34 and 0.50 V are assigned to the phase transition between amorphous Li_xSi and amorphous Si [26]. Compared to the CNT@mp-Si electrode, mp-Si nanotube electrode showed a higher charge capacity (3,191 $mA·g^{-1}$) but a poor discharge capacity (1,351 $mA·g^{-1}$) with low coulombic efficiency (42.3%). Further dramatic capacity fading is observed after the second cycle (Fig. 4(b)). After the 100th cycle, the CNT@mp-Si electrode showed a capacity of 1,310 $mA·g^{-1}$ (i.e., 99% of the second cycle capacity) with coulombic efficiencies of 99%, whereas the mp-Si nanotube electrode exhibited poor cycling performance (Fig. 4(c)). The rate capability of the CNT@mp-Si electrode at various current densities is shown in Fig. 4(d) (delithiation: 200 $mA·g^{-1}$; lithiation: 200, 500, 1,000, 2,000, 4,000, 8,000, and 200 $mA·g^{-1}$). The discharge capacities of the fifth cycle at each current density are 1,798, 1,502, 1,385, 1,212, 991, and 685 $mAh·g^{-1}$ at 200, 500, 1,000, 2,000, 4,000, and 8,000 $mA·g^{-1}$, respectively. When the charge current is reduced to 200 $mA·g^{-1}$, the reversible capacity recovers to 1,640 $mAh·g^{-1}$. To further evaluate the long-term stability of the CNT@mp-Si electrode, an electrochemical test was conducted at 1,000 $mA·g^{-1}$ for 300 cycles (Fig. 4(e)). The activation process was introduced during the initial two cycles (200 and 500 $mA·g^{-1}$). The capacity of the CNT@mp-Si electrode was well maintained up to 300 cycles, and the discharge capacity was 1,019 $mAh·g^{-1}$, corresponding to a coulombic efficiency of 99.6%, after 300 cycles. The obtained cycle performance is comparable to or even better than those of well-aligned CNT@Si and CNT@Si@C electrodes prepared by chemical vapor deposition (CVD) or physical vapor deposition (PVD) [10–12, 31, 32]. The highly efficient channels for rapid transport of electrons and Li ions and the balanced open voids that allow the free expansion of Si while maintaining structural

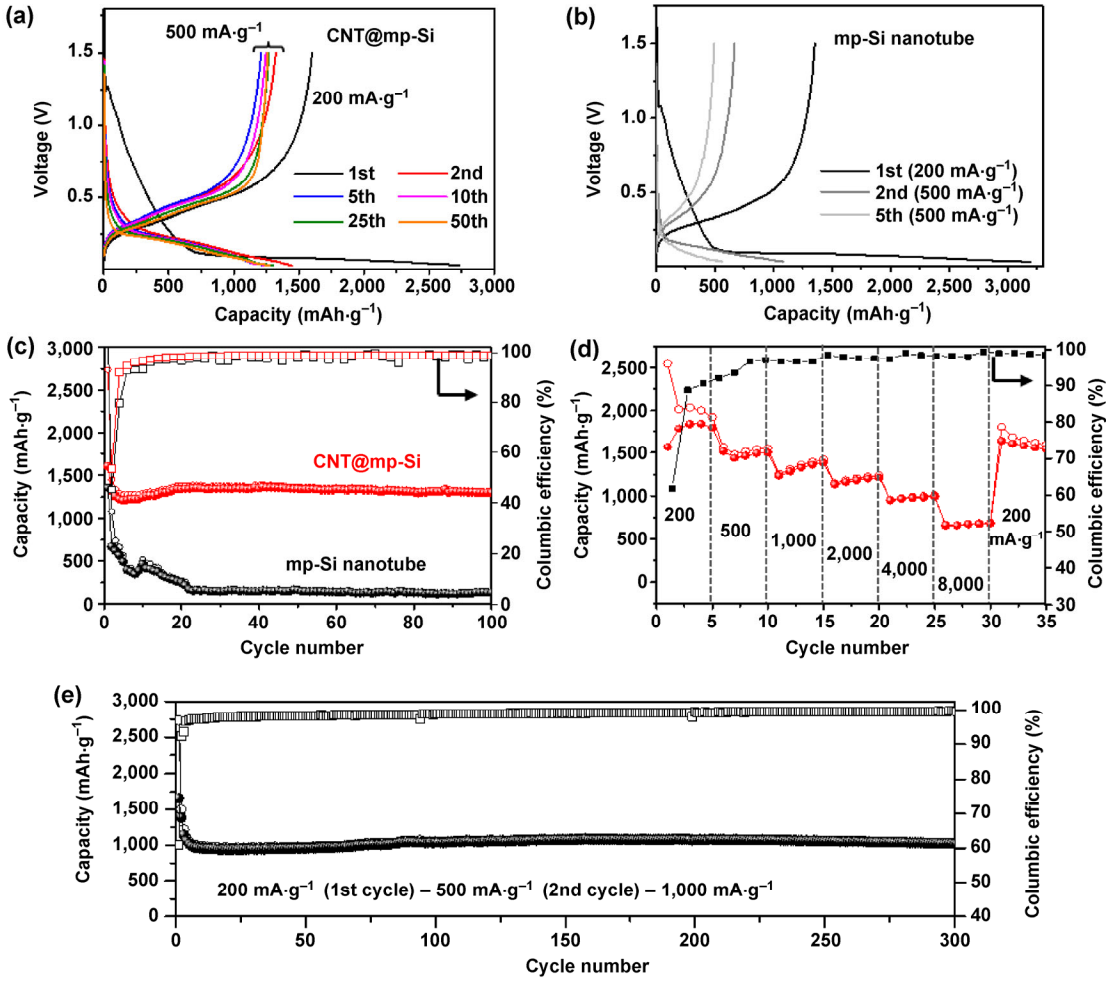

Figure 4 (a) Voltage profile of the CNT@mp-Si electrode over a potential range of 0.04–1.5 V at 500 mA·g^{-1}. (b) Voltage profile of the mp-Si nanotube electrode over a potential range of 0.04–1.5 V at 500 mA·g^{-1}. (c) Cycling test of CNT@mp-Si and mp-Si nanotube electrodes at 500 mA·g^{-1}. (d) Rate capability of CNT@mp-Si (delithiation: 200 mA·g^{-1}; lithiation: 200, 500, 1,000, 2,000, 4,000, 8,000, and 200 mA·g^{-1}). (e) Cycling test of CNT@mp-Si at 1,000 mA·g^{-1} for 300 cycles.

integrity have been reported to be necessary to achieve enhanced electrochemical performance [18]. In this respect, CNT@mp-Si was found to be an excellent anode material for LIBs. In addition, increasing the Si shell thickness to 600 nm was observed to result in poor cycling performance without increased capacity (see the ESM, Fig. S9), and thus, based on these results, a Si shell thickness of 200 nm was determined to be optimal for CNT/mp-Si electrode.

To determine the changes in the structures and morphologies of the CNT@mp-Si electrode during cycling, the coin cell was dissembled, and the morphology was investigated by SEM. No remarkable morphology change or severe crack/fracture was observed after 100 cycles at 500 mA·g^{-1}, and the surface was smooth compared to that of the pristine electrode (Figs. 5(a)–5(c)). To further demonstrate the structural stability of CNT@mp-Si, the dissembled electrode was rinsed with dimethyl carbonate (DMC) and D.I. water and then observed by SEM. Figure 5(d) shows the morphology of the CNT@mp-Si electrode lithiated to 0.04 V (1st cycle) at 200 mA·g^{-1}. The meso-porous surface of CNT@mp-Si became smooth because of Li-Si alloy and SEI layer formation during lithiation. The meso-porous structure reappeared in the electrode delithiated to 1.5 V (1st cycle) (Fig. 5(e)). No apparent morphology change was observed. The 1-D structure persisted in the delithiated electrode after 100 cycles, but individual CNT@mp-Si nanoparticles merged via Li-assisted welding [33]. The CNT@mp-Si electrode's

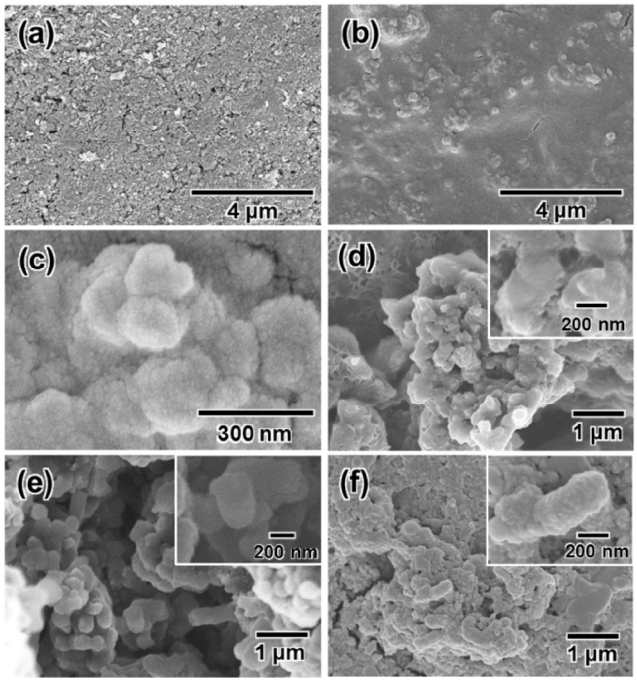

Figure 5 SEM images of the CNT@mp-Si electrode: (a) pristine and (b) and (c) after 100 cycles at 500 $mA \cdot g^{-1}$. SEM images of rinsed electrodes: (d) electrode lithiated to 0.04 V (1st cycle) at 200 $mA \cdot g^{-1}$, (e) electrode delithiated to 1.5 V (1st cycle) at 200 $mA \cdot g^{-1}$, and (d) delithiated electrode after 100 cycles at 500 $mA \cdot g^{-1}$.

morphology after 300 cycles at 1,000 $mA \cdot g^{-1}$ was also examined. More cracks were found, but no severe fracture was observed (see the ESM, Fig. S10). These results confirm that the meso-porous Si structure can accommodate the large volume change during lithiation/delithiation.

4 Conclusions

In summary, a CNT@mp-Si composite was successfully prepared by combining magnesiothermic reduction and acid etching. The electrochemical test revealed that the CNT@mp-Si electrode exhibited excellent cycle and rate performance as an anode for LIBs because the meso-porous Si structure efficiently accommodates the volume change and the CNT core contributes enhanced electrical conductivity. The observed cycle performance of the CNT@mp-Si electrode was comparable to or even better than that of well-aligned CNT@Si prepared by vapor deposition. This work confirms that magnesiothermic reduction is a scalable process for the large-scale production of Si nanostructures, which can be utilized in a variety of applications, such as LIBs, photocatalysis, and photoelectrochemical cells (PECs) for water splitting.

Acknowledgements

This work was supported by the National Research Foundation of Korea (NRF) grant funded by the Korea government (MEST) (No. 2012-008226).

Electronic Supplementary Material: Supplementary material (annealing schedule, optical micrographs of burst reaction, thermogravimetric analysis, XRD pattern and SEM images of mp-Si nanotubes, cyclic voltammetry curve of CNT@mp-Si electrode) is available in the online version of this article at http://dx.doi.org/10.1007/s12274-016-1106-x.

References

[1] Obrovac, M. N.; Christensen, L. Structural changes in silicon anodes during lithium insertion/extraction. *Electrochem. Solid-State Lett.* **2004**, *7*, A93–A96.

[2] Green, M.; Fielder, E.; Scrosati, B.; Wachtler, M.; Serra Moreno, J. Structured silicon anodes for lithium battery applications. *Electrochem. Solid-State Lett.* **2003**, *6*, A75–A79.

[3] Kim, H.; Seo, M.; Park, M.-H.; Cho, J. A critical size of silicon nano-anodes for lithium rechargeable batteries. *Angew. Chem., Int. Ed.* **2010**, *49*, 2146–2149.

[4] Chan, C. K.; Peng, H. L.; Liu, G.; McIlwrath, K.; Zhang, X. F.; Huggins, R. A.; Cui, Y. High-performance lithium battery anodes using silicon nanowires. *Nat. Nanotechnol.* **2008**, *3*, 31–35.

[5] Jing, S. L.; Jiang, H.; Hu, Y. J.; Li, C. Z. Directly grown Si nanowire arrays on Cu foam with a coral-like surface for lithium-ion batteries. *Nanoscale* **2014**, *6*, 14441–14445.

[6] Chen, D. Y.; Mei, X.; Ji, G.; Lu, M. H.; Xie, J. P.; Lu, J. M.; Lee, J. Y. Reversible lithium-ion storage in silver-treated nanoscale hollow porous silicon particles. *Angew. Chem., Int. Ed.* **2012**, *51*, 2409–2413.

[7] Kim, W.-S.; Hwa, Y.; Shin, J.-H.; Yang, M.; Sohn, H.-J.; Hong, S.-H. Scalable synthesis of silicon nanosheets from sand as an anode for Li-ion batteries. *Nanoscale* **2014**, *6*, 4297–4302.

[8] Jing, S. L.; Jiang, H.; Hu, Y. J.; Li, C. Z. Graphene supported mesoporous single crystal silicon on Cu foam as a stable lithium-ion battery anode. *J. Mater. Chem. A* **2014**, *2*, 16360–16364.

[9] Hwa, Y.; Kim, W.-S.; Hong, S.-H.; Sohn, H.-J. High capacity and rate capability of core–shell structured nano-Si/C anode for Li-ion batteries. *Electrochim. Acta* **2012**, *71*, 201–205.

[10] Evanoff, K.; Khan, J.; Balandin, A. A.; Magasinski, A.; Ready, W. J.; Fuller, T. F.; Yushin, G. Towards ultrathick battery electrodes: Aligned carbon nanotube—Enabled architecture. *Adv. Mater.* **2012**, *24*, 533–537.

[11] Fan, Y.; Zhang, Q.; Xiao, Q. Z.; Wang, X. H.; Huang, K. High performance lithium ion battery anodes based on carbon nanotube–silicon core–shell nanowires with controlled morphology. *Carbon* **2013**, *59*, 264–269.

[12] Wang, W.; Epur, R.; Kumta, P. N. Vertically aligned silicon/carbon nanotube (VASCNT) arrays: Hierarchical anodes for lithium-ion battery. *Electrochem. Comm.* **2011**, *13*, 429–432.

[13] Cui, L.-F.; Hu, L. B.; Choi, J. W.; Cui, Y. Light-weight free-standing carbon nanotube-silicon films for anodes of lithium ion batteries. *ACS Nano* **2010**, *4*, 3671–3678.

[14] Chou, S.-L.; Zhao, Y.; Wang, J.-Z.; Chen, Z.-X.; Liu, H.-K.; Dou, S.-X. Silicon/single-walled carbon nanotube composite paper as a flexible anode material for lithium ion batteries. *J. Phys. Chem. C* **2010**, *114*, 15862–15867.

[15] Evanoff, K.; Benson, J.; Schauer, M.; Kovalenko, I.; Lashmore, D.; Ready, W. J.; Yushin, G. Ultra strong silicon-coated carbon nanotube nonwoven fabric as a multifunctional lithium-ion battery anode. *ACS Nano* **2012**, *6*, 9837–9845.

[16] Hu, L. B.; Liu, N.; Eskilsson, M.; Zheng, G. Y.; McDonough, J.; Wågberg, L.; Cui, Y. Silicon-conductive nanopaper for Li-ion batteries. *Nano Energy* **2013**, *2*, 138–145.

[17] Hu, L. B.; Wu, H.; Gao, Y. F.; Cao, A. Y.; Li, H. B.; McDough, J.; Xie, X.; Zhou, M.; Cui, Y. Silicon–carbon nanotube coaxial sponge as Li-ion anodes with high areal capacity. *Adv. Energy Mater.* **2011**, *1*, 523–527.

[18] Jing, S. L.; Jiang, H.; Hu, Y. J.; Shen, J. H.; Li, C. Z. Face-to-face contact and open-void coinvolved Si/C nano-hybrids lithium-ion battery anodes with extremely long cycle life. *Adv. Funct. Mater.* **2015**, *25*, 5395–5401.

[19] Bao, Z. H.; Weatherspoon, M. R.; Shian, S.; Cai, Y.; Graham, P. D.; Allan, S. M.; Ahmad, G.; Dickerson, M. B.; Church, B. C.; Kang, Z. T. et al. Chemical reduction of three-dimensional silica micro-assemblies into microporous silicon replicas. *Nature* **2007**, *446*, 172–175.

[20] Jia, H. P.; Gao, P. F.; Yang, J.; Wang, J. L.; Nuli, Y.; Yang, Z. Novel three-dimensional mesoporous silicon for high power lithium-ion battery anode material. *Adv. Energy Mater.* **2011**, *1*, 1036–1039.

[21] Yoo, J.-K.; Kim, J.; Jung, Y. S.; Kang, K. Scalable fabrication of silicon nanotubes and their application to energy storage. *Adv. Mater.* **2012**, *24*, 5452–5456.

[22] Feng, X. J.; Yang, J.; Bie, Y. T.; Wang, J. L.; Nuli, Y.; Lu. W. Nano/micro-structured Si/CNT/C composite from nano-SiO_2 for high power lithium ion batteries. *Nanoscale* **2014**, *6*, 12532–12539.

[23] Zhu, X. F.; Xia, B. Y.; Guo, M. Y.; Zhang, Q.; Li, J. X. Synthesis of carbon nanotube composites with size-controlled silicon nanoparticles. *Carbon* **2010**, *48*, 3296–3299.

[24] Choi, S.; Lee, J. C.; Park, O.; Chun, M.-J.; Choi, N.-S.; Park, S. Synthesis of micro-assembled Si/titanium silicide nanotube anodes for high-performance lithium-ion batteries. *J. Mater. Chem. A* **2013**, *1*, 10617–10621.

[25] Lipson, A. L.; Chattopadhyay, S.; Karmel, H. J.; Fister, T. T.; Emery, J. D.; Dravid, V. P.; Thackeray, M. M.; Fenter, P. A.; Bedzyk, M. J.; Hersam, M. C. Enhanced lithiation of doped 6H silicon carbide (0001) via high temperature vacuum growth of epitaxial graphene. *J. Phys. Chem. C* **2012**, *116*, 20949–20957.

[26] Liu, N.; Huo, K. F.; McDowell, M. T.; Zhao, J.; Cui, Y. Rice husks as a sustainable source of nanostructured silicon for high performance Li-ion battery anodes. *Sci. Rep.* **2013**, *3*, 1919.

[27] Li, H.; Huang, X. J.; Chen, L. Q.; Zhou, G. W.; Zhang, Z.; Yu, D. P.; Mo, Y. J.; Pei, N. The crystal structural evolution of nano-Si anode caused by lithium insertion and extraction at room temperature. *Solid State Ionics* **2000**, *135*, 181–191.

[28] Li, J.; Dahn, J. R. An *in situ* X-ray diffraction study of the reaction of Li with crystalline Si. *J. Electrochem. Soc.* **2007**, *154*, A156–A161.

[29] Netz, A.; Huggins, R. A.; Weppner, W. The formation and properties of amorphous silicon as negative electrode reactant in lithium systems. *J. Power Sources* **2003**, *119–121*, 95–100.

[30] Hatchard, T. D.; Dahn, J. R. *In situ* XRD and electrochemical study of the reaction of lithium with amorphous silicon. *J. Electrochem. Soc.* **2004**, *151*, A838–A842.

[31] Wang, W.; Ruiz, I.; Ahmed, K.; Bay, H. H.; George, A. S.; Wang, J.; Butler, J.; Ozkan, M.; Ozkan, C. S. Silicon decorated cone shaped carbon nanotube clusters for lithium ion battery anodes. *Small* **2014**, *10*, 3389–3396.

[32] Wang, W.; Kumta, P. N. Nanostructured hybrid silicon/carbon nanotube heterostructures: Reversible high-capacity lithium-ion anodes. *ACS Nano* **2010**, *4*, 2233–2241.

[33] Karki, K.; Epstein, E.; Cho, J.-H.; Jia, Z.; Li, T.; Picraux, S. T.; Wang, C. S.; Cumings, J. Lithium-assisted electrochemical welding in silicon nanowire battery electrodes. *Nano Lett.* **2012**, *12*, 1392−1397.